DIII-D Contributions Toward the Scientific Basis
for Sustained Burning Plasmas

C.M. Greenfield and the DIII-D Team

General Atomics, San Diego, California, USA

e-mail contact of main author: greenfield@fusion.gat.com

Abstract. DIII-D is making significant contributions to a scientific basis for sustained burning plasma operation. These include explorations of increasingly reactor relevant scenarios, studies of key issues for projecting performance, development of techniques for handling heat and particle efflux, and assessment of key issues for the ITER Research Plan. Steady-state scenarios are generated and maintained for a duration limited by hardware, using tailoring of the early evolution and precise targeting of external current drive. Joint DIII-D/JET $\rho*$ scans in the hybrid regime imply Bohm-like confinement scaling. Startup and shutdown techniques were developed for the restrictive environment of future devices while retaining compatibility with advanced scenarios. Toward the goal of a fully predictive capability, the DIII-D program emphasizes validation of physics-based models, facilitated by a number of new and upgraded diagnostics. Specific areas include transport, rotation, energetic particles, and the H-mode pedestal, but this approach permeates the entire research program. Concerns for heat and particle efflux in future devices are addressed through studies of ELM control, disruption avoidance and mitigation, and hydrogenic retention in DIII-D's carbon wall. DIII-D continues to respond to specific needs for ITER. Recent studies have compared H-mode access in several different ion species, identifying not only isotopic, but density, rotation, and geometrical dependencies that may guide access to H-mode during ITER's non-activated early operation. DIII-D used an insertable module to simulate the magnetic perturbations introduced by one of ITER's three Test Blanket Module sets, demonstrating that little impact on performance is seen at ITER equivalent levels of magnetic perturbation.

1. Introduction

DIII-D research is contributing to the scientific basis for the optimization of the tokamak approach to fusion energy production. Ensuring the success of ITER remains a major priority of the program, as its needs evolve from specific short-term design issues toward longer-term concerns for ITER research planning. For longer-term success of ITER, and indeed of future devices up to and including a power plant, DIII-D research works toward scientific understanding across a range of research areas. The results of these endeavors will be embodied in reliable predictive tools that can be applied toward design of devices and experiments.

In this paper, we will summarize recent research contributing to these goals. DIII-D research continues advance development, characterization and access to operating scenarios of interest and importance for burning plasmas (Sec. 2). Relying on DIII-D's comprehensive set of control tools and diagnostics, a vigorous research program is underway to carry out specific tests of physics-based models of transport, rotation, energetic particle effects, and the H-mode pedestal (Sec. 3). Methods for handling heat and particle efflux, including transients [edge localized modes (ELMs) and disruptions] and tritium retention, are described in Sec. 4. DIII-D continues to be responsive to the specific needs of ITER. Two of these needs, isotope dependence of the L-H threshold and the plasma response to Test Blanket Modules (TBMs), are described in Sec. 5. In Sec. 6, we will briefly discuss new capabilities being added to DIII-D and the future research directions that will be enabled.

2. Scenario Development, Characterization, and Access

2.1 High-beta Steady-state Scenario Optimization

To assess the optimum q profile for discharges in DIII-D with 100% of the current driven noninductively ($f_{NI} = 1$), the self-consistent response of the plasma profiles to changes in the q profile was studied in high f_{NI}, high β_N discharges through a scan of q_{min} and q_{95} at two values of β_N [1,2]. As expected, both the bootstrap current fraction, f_{BS}, [Fig. 1(a)] and f_{NI} increased with q_{95}. The temperature and density profiles were found to broaden as either q_{min} or β_N is increased [Fig. 1(b)], thereby preventing the expected increase in f_{BS} at the highest values of

q_{min}. The changes in the shapes of the profiles at high β_N modify the bootstrap current density profile from peaked close to the axis to relatively flat between the axis and the H-mode pedestal. Therefore, significant externally driven current is required in the region inside the H-mode pedestal to match the profiles of the noninductive current density (J_{NI}) to the desired total current density (J). In this experiment, the additional current density was provided mostly by neutral beam current drive. The profiles of J_{NI} and J were most similar at $q_{min} \approx 1.35$–1.65,

FIG. 1. The (a) bootstrap fraction f_{BS} and (b) pressure peaking factor $f_p = \left[n_e(0)T_e(0) + n_i(0)T_i(0) \right] / \langle n_e T_e + n_i T_i \rangle$ both depend on the q profile, characterized here by q_{core} [$q(\rho)$ averaged over $0 < \rho < 0.3$] and q_{95}. The open symbols are from a set of discharges with neutral beam injection (NBI) controlled to maintain $\beta_N \approx 2.8$. The discharges shown with filled symbols in (b), heated by the maximum available power $P_{NBI} = 13.5$ MW, indicate the broadening of the profile seen at high β_N.

$q_{95} \approx 6.8$, where f_{BS} is also maximum, establishing this q profile as the optimal choice for $f_{NI}=1$ operation in DIII-D with the existing set of external current drive sources.

These experiments focused on establishing the desired conditions for a sustained scenario, but not on actual sustainment. This will require replacement of inductively driven current driven near the half-radius [3]. Presently, this current is primarily provided by electron cyclotron current drive (ECCD). Modifications now underway will make off-axis neutral beam current drive (NBCD) and additional ECCD available for future experiments.

In previous experiments, the high β phase often terminated with the onset of n=1 tearing modes due to small departures of the current profile from an otherwise stable target. This motivates fine tuning of the ECCD deposition profile. Recently, we scanned the position and width of the ECCD (by separately aiming six gyrotrons) and determined that broad deposition near the q=2 surface improves both the duration and reproducibility of the high f_{NI}, high β_N condition. Figure 2 shows two similar discharges with different aiming. When ECCD is aimed broadly just outside the q=2 surface, high performance is maintained for the duration of the ECCD pulse. Aiming at larger radius, near $q \approx 3$, produces substantially less ECCD (by about an order of magnitude) due to lower T_e, and the high β phase is terminated earlier by a tearing mode.

Plasmas in the steady-state scenario often have β_N above the no-wall stability limit. Recent research has identified kinetic effects as important for stability in this regime, even in non-rotating plasmas [4,5].
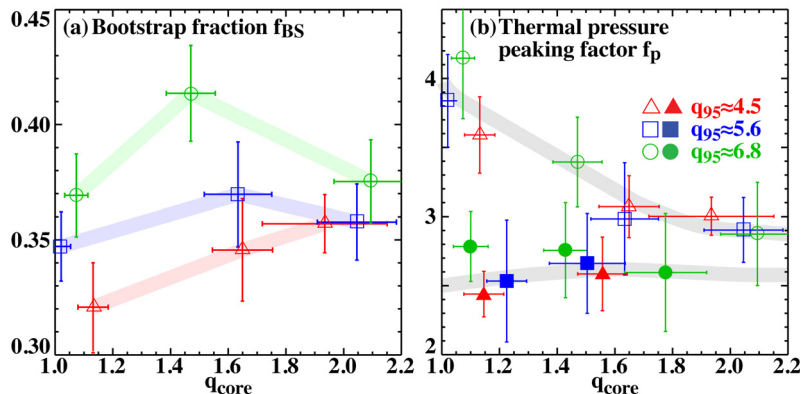

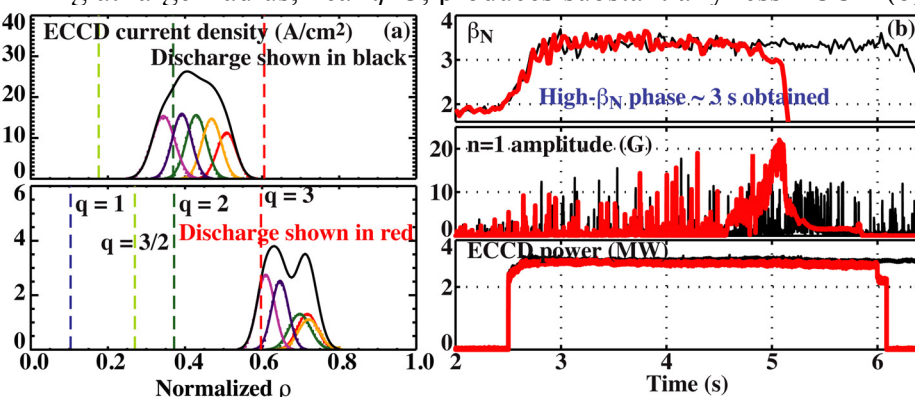FIG. 2. (a) ECCD deposition profiles for two otherwise similar discharges with $f_{NI} \approx 100\%$. Colored curves represent the contributions from individual gyrotrons, and the black curve represents the total ECCD. (b) Time histories indicating that the high β phase of the discharge with ECCD deposition outside the q=3 radius is terminated by the onset of an n=1 tearing mode. Deposition at a smaller radius extends the high β phase until after the ECCD pulse ends.

2.2 Confinement in Advanced Inductive Scenarios

Advanced inductive (AI) plasmas are a realization of the ITER hybrid scenario, providing high neutron fluence in a prolonged inductive discharge. The AI scenario has been studied less extensively than conventional H-mode, leaving uncertainty in extrapolation to ITER. DIII-D and JET [6] have recently performed a joint experiment to determine the dependence of confinement on several key parameters [7]. The largest extrapolation to ITER is in its size, expressed in dimensionless quantities as $\rho*$, the normalized ion gyroradius evaluated at normalized radius $\rho=0.5$. In this experiment, the two devices spanned a range of 2.7 in $\rho*$, considerably larger than is possible in any single device and about equal to the difference between JET and ITER. To carry out these experiments, plasmas with the same shape and aspect ratio were produced in both tokamaks.

FIG. 3. Normalized energy confinement $B\tau_E$ vs. $\rho*$ (closed symbols). The dependence on q_{cyl} and β, from the ITER98(y,2) scaling, is included to account for small residual variations in q and β in the data. $H_{98y,2}$ shown in open symbols.

Linear dimensions of the plasma in JET were larger by a factor of 1.67 compared to DIII-D. As closely as possible, dimensionless parameters other than $\rho*$ were matched to those expected in ITER and well matched between JET and DIII-D. The global energy confinement was found to be roughly Bohm-like (Fig. 3). Over the same range, the confinement normalized to the ITER98(y,2) follows the scaling relation $H_{98(y,2)} \approx 1.2–1.3$, and does not vary with $\rho*$.
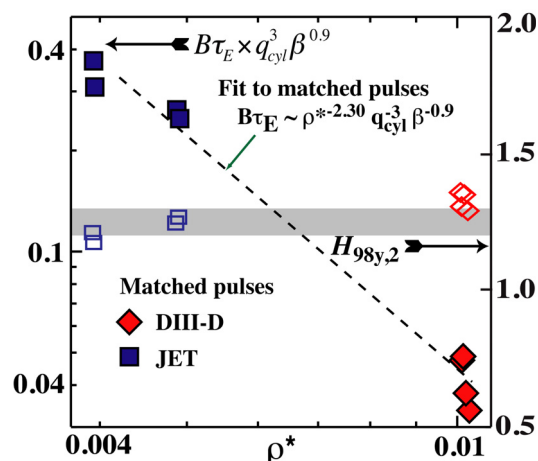
2.3. Access to and Safe Shutdown from ITER Operating Scenarios

DIII-D is developing and demonstrating startup, ramp-up, and ramp-down scenarios that are compatible with ITER's restrictive environment and capable of producing appropriate target conditions for several ITER operating scenarios. Low breakdown voltages have been achieved with (≥ 0.21 V/m, lower than the maximum 0.3 V/m for ITER) and without (≥ 0.42 V/m) assistance from ECH. Transitioning to a large bore divertor configuration early in the current ramp reduces heat flux to poloidal limiters, and allows control of the internal inductance l_i by varying the current ramp rate. Efforts to model the current ramp phase with CORSICA have successfully matched the evolution of T_e and q near the axis, but have so far not successfully matched the current profile.

These ramp-up and ramp-down scenarios have been combined into a single discharge [8], with a flattop in the ITER baseline (conventional H-mode) scenario (Fig. 4). Similar demonstrations have been carried out in Ohmic and Hybrid scenario discharges.
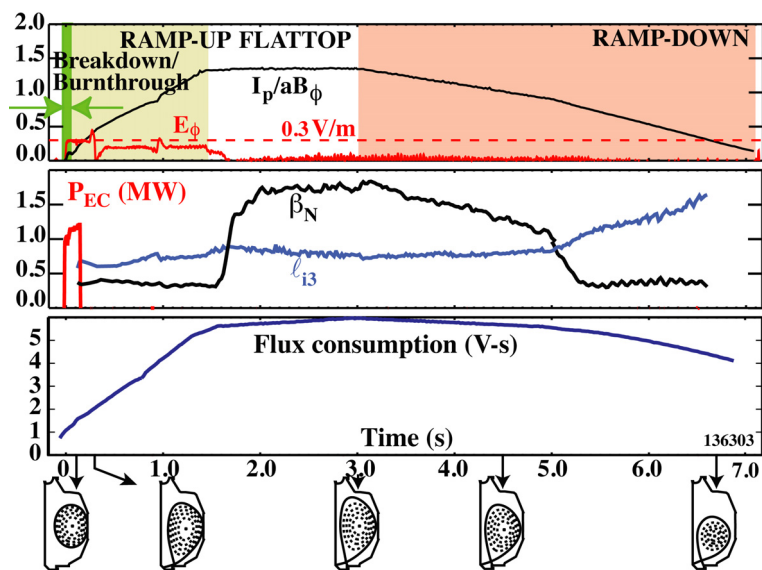

FIG. 4. An ITER baseline scenario discharge achieved with startup, ramp-up, and ramp-down scenarios optimized for the restrictions anticipated in future devices.

DIII-D experiments have demonstrated that full rampdown can be achieved with no additional transformer flux. We find that a controlled elongation rampdown is effective at preventing uncontrolled density increases that might trigger a disruption. The ITER rampdown scenario is terminated by exceeding the vertical control limit, in agreement with calculations. However, the termination occurs reproducibly below the ITER equivalent current level of 1.4 MA, where arbitrary disruptivity rates are allowed.

DIII-D discharges have been developed to simulate the remaining leading operational scenarios for ITER, and detailed modeling of these experiments is in progress [9].

3. Improved Physics Basis for Performance Projections

3.1 Transport Model Validation

Detailed validation studies underway at DIII-D aim to test physics-based transport models in L-mode [10–12], H-mode, and QH-mode [13] plasmas. "Validation studies" refers to a process comparing measurements to simulated values to assess the models' accuracy. Fluctuation diagnostics for multiple fields (e.g., n_e and T_e) spanning a wide range of spatial scales ($k_\theta \rho_s \approx 0.1$ to >10), and simulations (e.g. GYRO [14]) have advanced sufficiently to make such studies viable. Essential to these comparisons are synthetic diagnostics, digital analogues of real diagnostics applied to the output of the models.

FIG. 5. Relative change in fluctuation levels at $\rho=0.6$ as T_e is increased by adding ECH. The measurements are made by correlation ECE (CECE), beam emission spectroscopy (BES), Doppler backscattering (DBS), and high-k backscattering (HKBS).

One such study is a recent L-mode T_e/T_i scan [10], where electron cyclotron heating (ECH) was applied to a NBI-heated L-mode plasma, with a resulting 50% increase in T_e in the mid-core region of interest ($0.5 \leq \rho \leq 0.8$). Figure 5 shows the resulting change in measured fluctuation levels at $\rho=0.6$. A large increase is seen in low-k $\tilde{T}_e/T_e$, in qualitative agreement with nonlinear GYRO. Within experimental uncertainties, no change is observed in low through high-k $\tilde{n}_e/n_e$. GYRO predictions appear consistent with this at low-k. High-k simulations have not yet been performed. GYRO simulated thermal fluxes (not shown) are in qualitative agreement with experiment, with substantial, but incomplete, quantitative agreement [10]. Recent GYRO calculations at $\rho=0.8$ either do not converge or undergo numerical instabilities, indicating a possible need for coupled low through high-k multiple modes nonlinear simulations; this is currently under investigation. These observations fit a general trend in DIII-D that simulated transport and fluctuation levels in the mid-core region ($\rho\approx0.5$) are often in better agreement with experiment than those in the outer region ($\rho>0.75$), where edge effects may be important [10]. Results such as these are noteworthy as they point to potential future research paths.

3.2 Edge Momentum Source for Intrinsic Rotation During H-mode

DIII-D is also working toward a predictive understanding of rotation, with recent emphasis on drive mechanisms. The main source of momentum in DIII-D is neutral beams, but driving large rotation in ITER and other future tokamaks via NBI will be challenging at best. "Intrinsic" rotation has been observed in several devices, including DIII-D, but is not well understood. DIII-D experiments previously inferred an "intrinsic torque" in the edge [15]. However, identification of the driving mechanism has still been missing.

Recently, a strongly co-rotating layer has been observed with a reciprocating multi-tip Langmuir probe just inside the separatrix of H-mode discharges [16] (Fig. 6). The 1-cm-wide layer forms independently of injected torque less than 50 ms after an L-H transition. In pure ECH plasmas with no applied torque, the flat core rotation profile spins up over 600 ms to
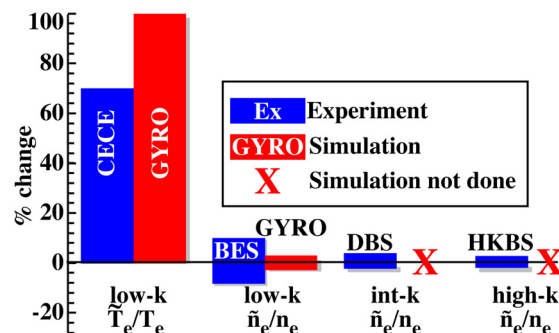
match the edge rotation layer's velocity (~35 km/s). This indicates that the layer is a cause, rather than effect, of core rotation and that viscous transport down the layer's gradient can slowly spin up the core. A simple orbit loss model [17] successfully reproduces the layer's profile shape, suggesting a link between these losses and formation of the layer.

The total toroidal-radial Reynolds stress [18] is essentially zero outside the layer's peak and becomes increasingly positive further inward. It thus acts to oppose the spin-up of the core by transporting momentum outward, directed up the layer's gradient, thereby helping to maintain the peaked shape over long timescales. This calls into question the role of Reynolds stress in the physics of the edge rotation layer.

3.3 Rotation Driven by Dominantly Non-Resonant Magnetic Fields

In recent experiments in DIII-D, the first observation of a theoretically-predicted peak in the neoclassical toroidal viscosity (NTV) torque for low toroidal rotation rates has been made [19] (Fig. 7). We have previously reported observations that static, dominantly non-resonant, $n=3$ fields apply a torque to the plasma that drives it toward a counter-rotating (opposite to the plasma current) finite velocity [20]. This effect is predicted by NTV theory [21], and can be accessed through application of these fields from internal coils (the I-coil) in DIII-D. In the present experiment, a series of similar discharges was prepared, scanning over a range of toroidal rotation rates Ω. The neutral beams are feedback controlled to maintain constant values of β_N and Ω, so that they will respond to additional torques applied by other sources. An $n=3$ field is applied by activating the I-coil, and the NTV torque determined by the change in NBI torque required to maintain the programmed value of Ω: $\Delta T_{NBI} = -T_{NTV}(\Omega)$. As shown in Fig. 7, the experimental data exhibits a peak in the torque centered at the location predicted by theory.
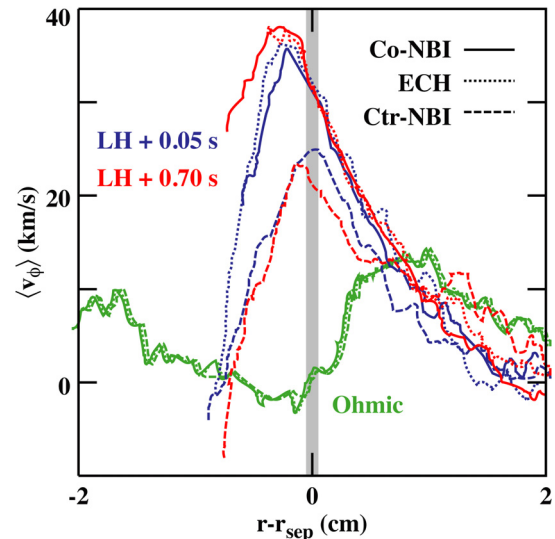

FIG. 6. An edge co-rotation layer forms immediately after the L-H transition and is maintained for the duration of the H-mode phase. The sign of this rotation is independent of the direction of applied torque.
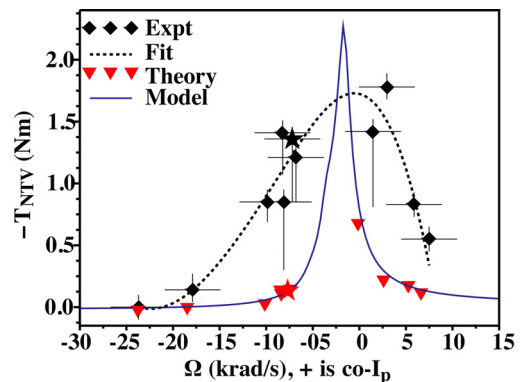

FIG. 7. Comparison of measured NTV (diamonds), and cylindrical torque model (line) vs deuterium toroidal rotation rate (obtained from NCLASS) at $\rho=0.67$. A least-squares spline fit (dashed) is shown for the data.

This torque can have practical benefits. QH-mode [22,23] exhibits performance comparable to the ITER Baseline ELMing H-mode, but without ELMs and their damaging effects. Its attractiveness has been limited by an operational requirement for strong NBI driven rotation, which cannot be anticipated in ITER or any reactor grade tokamak. In recent experiments, an $n=3$ field produced by combining the internal I- and external C-coils has been used to apply NTV torque to maintain edge rotation with zero net NBI torque [24]. In these cases, QH-mode was accessed via the usual counter-NBI technique, with the torque removed (by balancing the NBI) over about a 1 s interval. Following this, QH-mode operation with zero-net NBI torque was maintained for 1 s, until the $n=3$ field was removed (Fig. 8). Analysis indicates that E×B rotational shear, whether driven by NBI or NTV, may be the appropriate shear for theories explaining QH-mode access. In addition, the effect of applying predomi-

nantly nonresonant magnetic perturbations did not saturate at the highest perturbation amplitudes. This may open a plausible path to QH-mode utilization in ITER.

3.4 Improved Understanding of Energetic Particle (EP) Behavior

Anomalous energetic particle transport is an important, yet poorly understood, term in the power balance,

FIG. 8. (a) n=3 NTV is applied, via the internal I- and external C-coils, to a pre-existing QH-mode. QH-mode phase is maintained after the neutral beam driven torque is eliminated, with constant β_N and confinement quality. (b) Toroidal rotation profiles before (blue) and after (red) the NBI torque is removed.

making transport analysis challenging when this transport is large. This is a more serious concern in burning plasmas, where energetic α particles will be the primary heating source. These concerns motivate efforts to identify, understand, and ultimately control, this transport.

New diagnostics provide data to test models of EP instabilities and associated transport. Discrepancies between measured and theoretical EP profiles suggest that the EP population is depleted through both fine-scale turbulence and large-scale instabilities [e.g. Alfvén Eigenmodes (AEs) including toroidal AEs (TAE), and reversed shear AEs (RSAE) [25].

Two-dimensional imaging of the modes' internal structure provides unprecedented detail on the nonlinear interaction of EPs with the background plasma. In a recent experiment [26], RSAEs were excited by an off-axis minimum in the q profile. Figure 9 shows a comparison of an $n=4$ RSAE calculated by the TAE/FL [27] code [Fig. 9(a)] and observed via ECE imaging [Fig. 9(b)]. The distinct poloidal shearing seen here is not reproduced by ideal MHD codes. It is reproduced by TAE/FL simulations only when coupling between the mode and the fast ion population is included [Fig. 9(c-d)], indicating that this effect may cause the shearing.

FIG. 9. Imaging of T_e/T_e from RSAEs. (a) TAE/FL simulation (44.6 kHz) and (b) ECEI measurement (65.92 kHz) of n=4 RSAE modes. The discrepancy in frequency arises from omission of compressibility in the model and is consistent with the geodesic acoustic shift of the Alfvén continuum. (c-d) TAE/FL simulations without (c) and with (d) inclusion of coupling to the fast ion population.

The newly commissioned DIII-D fast ion loss detector (FILD) observes fluctuations in ion flux that are coherent at frequencies in the TAE/RSAE range (60–100 kHz) with the energy and pitch angle of lost ions; the enhanced losses occur when AE are present. When the measured pitch angle and energy are used to trace backward from the FILD aperture along a path, calculated by the ORBIT [38] code, the lost ions are found to originate from a location where AEs are known to exist. The FILD results allow us for the first time to directly associate fast-ion losses with AEs [25].
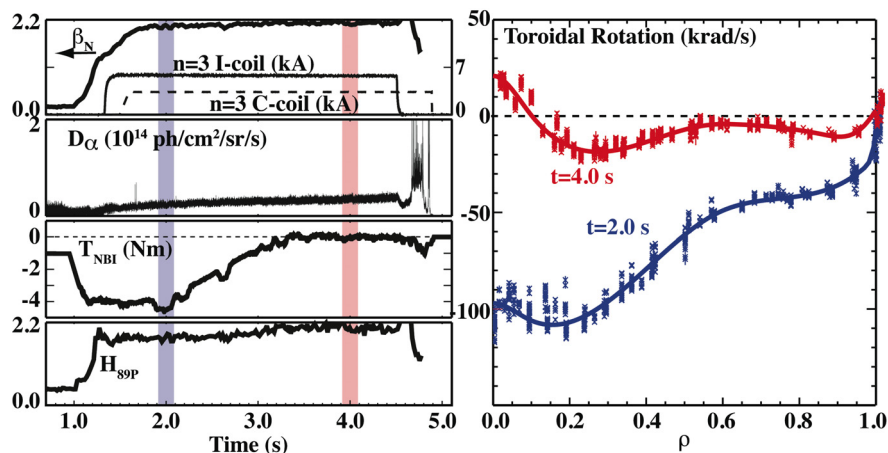
3.5 Predicting the H-mode Pedestal

Performance predictions for ITER and other future devices are strongly dependent on the structure and magnitude of the H-mode edge pedestal. Current models are beginning to yield more consistent predictions of the pedestal characteristics. Peeling-ballooning stability constrains the pedestal profile with the onset of ELMs, while the kinetic ballooning mode (KBM) has been proposed as a transport driving mechanism in the pedestal. These two phenomena are included in the EPED model, which has successfully matched observations on several tokamaks including DIII-D, JET, and JT-60U. The EPED1 model, however, required an empirically determined closure relation, $\Delta_{\psi N} \propto \beta_{p,ped}^{1/2}$, where $\Delta_{\psi N}$ is the pedestal width and

FIG. 10. Initial tests of the EPED1.6 model against data from DIII-D (squares), JET (circles), and C-Mod (triangles) are promising for improved confidence in predicting the pedestal in future experiments, such as ITER (diamond).

$\beta_{p,ped}$ is the poloidal β at the top of the pedestal. Recent improvements to the EPED model (EPED1.6) have eliminated this requirement by using a direct calculation of both P-B and KBM stability and no free parameters [29].

Pedestal heights measured on DIII-D, JET, and C-Mod are in good agreement with the first-principles based calculation of EPED1.6 (Fig. 10). Both versions of EPED give similar predictions for ITER, with a pedestal height of $\beta_{N,ped} \approx 0.6$ and width $\Delta\psi \approx 0.04$ (~4.4 cm). At ITER reference density, and typical peaking, $\beta_{N,ped} \approx 0.6$ corresponds to $T_{ped} \approx 4.1$ keV.

Additional research was performed jointly with JET to empirically determine the $\rho*$ scaling of the pedestal [30].

4. Heat and Particle Flux Control Methods

4.1 Reducing the Impact of ELMs

The impulsive heat load from ELMs is a major concern for ITER and other next step devices. DIII-D is exploring several techniques to eliminate or mitigate ELMs, including using resonant magnetic perturbations (RMPs) and ELM pacing by oscillating magnetic perturbation and pellet injection.

Peeling-ballooning stability calculations with the ELITE code [31] indicate that the RMP reduces the pedestal gradient below the P-B limit, presumably by increased transport. DIII-D research is focusing on elucidating the physical causes underlying that increase, so it can be better predicted and controlled.

A set of ELM-control coils is being considered for ITER based on empirical scaling from the vacuum stochastic layer applied in DIII-D experiments. We find the vacuum stochastic layer a useful proxy for a much more complex plasma response to the applied 3-D field. Figure 11 shows that a low-pressure region extends inward from the plasma edge with its extent corresponding to that of the vacuum stochastic layer [32].

During RMP experiments in high-β hybrid plasmas, the characteristics of ELM suppression were found consistent with those in standard H-modes [33]: The shape
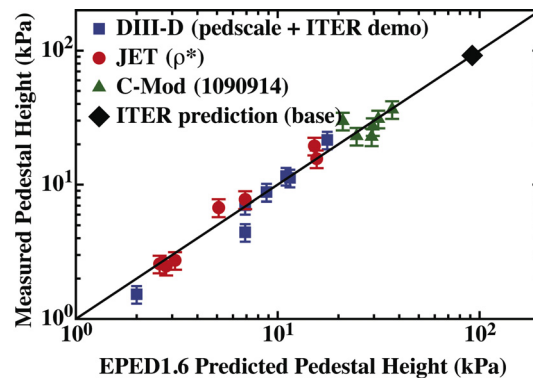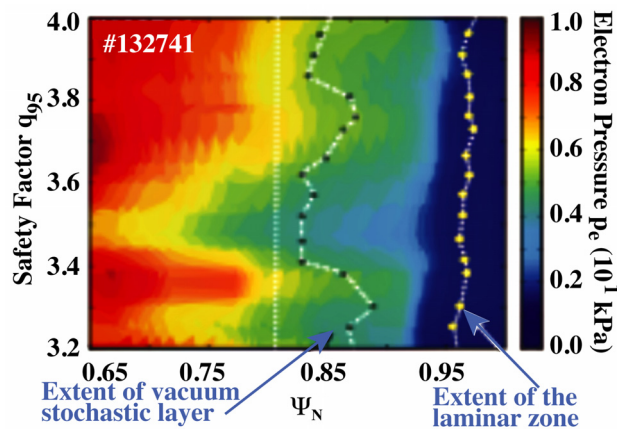

FIG. 11. DIII-D H-mode discharges show similar variations of electron pressure with the radial extent of the vacuum stochastic layer as q_{95} is varied over time.

and magnitude of the edge bootstrap current was observed to affect the confinement of magnetic field lines in the pedestal region, so that a larger bootstrap current separates magnetic resonant surfaces, reduces field line loss from the pedestal top, and correlates with a lack of ELM suppression.

We also observe that the RMP field directly affects low-k turbulence [34]. The core fluctuation amplitude measured by beam emission spectroscopy (BES) has been observed to modulate in phase with RMP amplitude during ELM suppression.

Although the impulsive heat load is of the greatest concern, it is desirable to be able to control the steady heat load as well. Experiments have been carried out to combine the beneficial effects of RMP ELM suppression and the radiative divertor, created by injecting gas into the divertor region. If sufficient power is radiated away, the divertor is said to "detach," e.g. appreciable heat is no longer conducted to the wall.

ELMs have not been fully suppressed by the RMP in combination with the gas puffing. However, as the pedestal density is increased, the divertor detaches, reducing the peak heat flux almost to the level of the ELM suppressed case [Fig. 12(a)]. The picture is very different if we consider the time averaged heat flux [Fig. 12(b)]. The RMP ELM suppressed case exhibits the *highest* heat flux now, where addition of the radiative divertor can reduce that to a very low level [35].

DIII-D is also researching pellet ELM pacing [36]. When small pellets are injected from the low field side of the plasma at 14 Hz, the ELM amplitude is reduced, and surprisingly, the resulting ELMs actually occur at an even *faster* rate (up to 25 Hz) than the pel-

FIG. 12. (a) Peak heat flux is reduced by RMP ELM suppression. Gas puffing in the divertor increases the peak, since ELMs have not been fully suppressed in that configuration. (b) The steady, time averaged, heat flux is highest with RMP ELM suppression, and is reduced with the addition of gas puffing.

let injection. This can be compared to a natural frequency of about 5 Hz. The small pellets do not penetrate the plasma and do not appreciably fuel the core. ELM pacing has been observed in phase with a 20 Hz modulation on the I-coil (the same coil as used for the RMP). The ELMs in this case are triggered at both the positive and negative peak, so the frequency is doubled.

4.2 Avoiding and Mitigating Disruptions

Rapid plasma shutdown via rapid particle delivery is being developed as a last-resort measure to mitigate disruption effects. This has two roles: First, to rapidly shut down the tokamak, and second, to quench the runaway electron (RE) beam that may form. The latter is very challenging due to the theoretically very high densities required. Also, NIMROD studies indicate MHD activity may be less effective in deconfining runaway electrons in ITER than in present tokamaks [37].
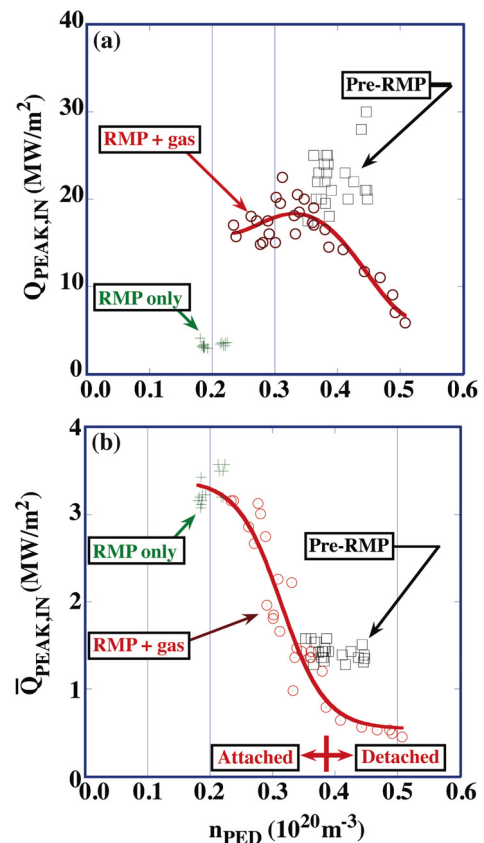
Previous studies concentrated on massive gas injection (MGI) from valves outside the plasma. These studies show that particle assimilation is only effective during the thermal quench; particles that arrive later, during the current quench, are ineffective. Recent experiments have explored shattered pellet injection (SPI) as an alternative particle delivery technique. A large deuterium pellet is injected into the DIII-D vessel, where it strikes a shatter plate, so that the resulting shards penetrate the plasma [38]. Although more localized than the effect of the MGI, SPI increases the core density to a higher level (as high as 9×10^{21} m^{-3}, a record density for DIII-D). The deuterium is delivered more rapidly than with MGI in the present valve configuration, though earlier experiments have shown that the MGI performance can be significantly improved by a higher throughput delivery system [39].

Detailed studies of the behavior of a RE beam produced by Ar pellet injection are underway. Figure 13 shows imaging of the beam during the arrival of a polystyrene pellet introduced as a probe [40]. As seen in Fig. 13(b), the pellet explodes outside the beam, suggesting volumetric heating. Also, the DIII-D plasma control system (PCS) can control the vertical position of the RE current channel, and the magnitude of the RE current via loop voltage. Based on these results, we can envision a scenario in which the RE beam undergoes a controlled ramp **down** following mitigation. Utilizing these capabilities, measurements have been made of the RE growth and decay rates, which are qualitatively consistent with those predicted by RE collisional drag theories.

4.3 Tritium Retention in Plasma Facing Components

Carbon is an appealing plasma facing material due to its heat tolerance. However, tritium retention is a serious concern for ITER. DIII-D research is working to quantify and develop techniques to counter retention.
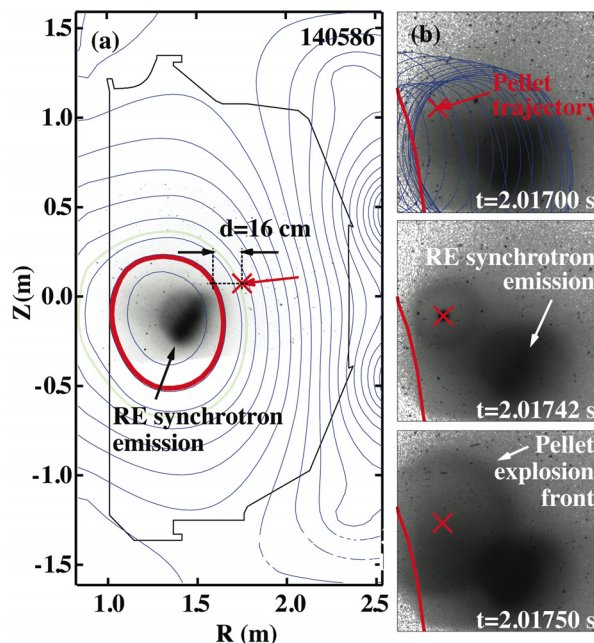
FIG. 13. Images of synchrotron emission from a runaway electron beam during injection of a polystyrene pellet injected as a probe. (a) The beam is located near the center of the DIII-D vessel, with the pellet injected from the low-field side of the plasma; (b) A series of snapshots spanning 0.5 ms, as the pellet arrives near the RE beam and explodes about 16 cm away from the last closed flux surface of the beam.

FIG. 14. Time histories of a pair of similar H-mode discharges, differing only in their heating source (ECH in red, NBI in black). (a) Plasma current, (b) line integrated density, (c) heating power, (d) particle input rate, (e) particle wall loading rate, (f) particle wall inventory.

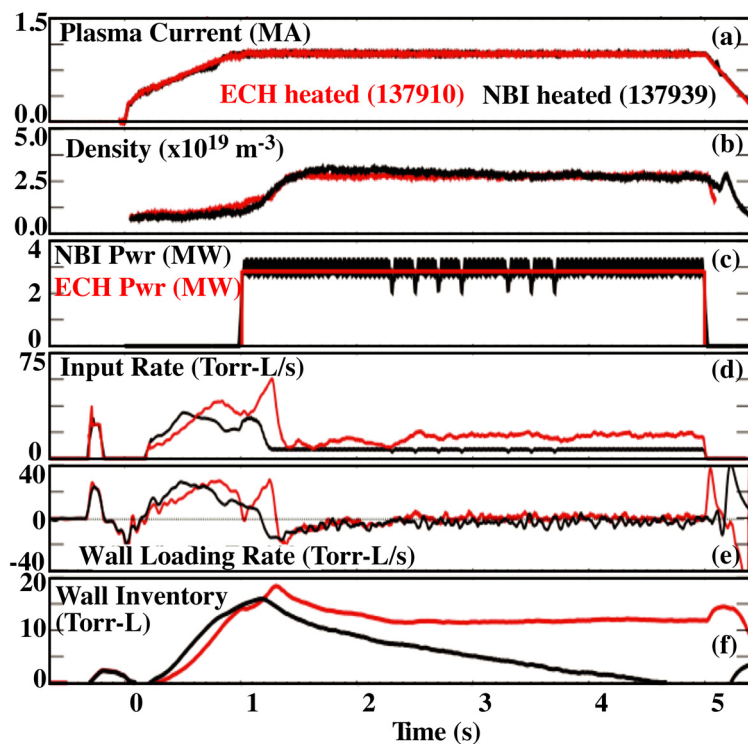Dynamic particle balance is shown for ECH and NBI heated H-mode discharges in Fig. 14. Although there is finite loading during the Ohmic and L-mode phases, surprisingly, the wall absorbs no additional particles during the H-mode. With NBI, particles are continually *removed* from the wall during H-mode, by the divertor cryopump, so the inventory at the beginning and end are the same.

This does not preclude hydrogen from being bound up with eroded carbon that redeposits at less exposed locations. DIII-D has tested thermal oxidation as a technique for removing these co-deposits. Prior to the experiment, an extensive laboratory testing program was carried out at the University of Toronto. The DIII-D vessel was then filled with a 10 torr $He:O_2$=90:10 mixture (~1 torr O_2 partial pressure) and baked for 2 hours at 350ºC, with pre-characterized sample tiles inserted. Estimates made by monitoring gas removed during and after the bake indicate about half of the co-deposits were removed. This result is consistent with expectations based on the lab tests. Following the bake, high performance hybrid plasmas were obtained after a short clean-up period. O_2 baking did not damage internal components, and did not compromise the vessel conditions needed for advanced scenarios [41].

5. Specific ITER Research Plan Issues

As ITER approaches its construction phase, DIII-D is increasing its emphasis on predictive understanding of physics governing ITER's behavior. However, DIII-D continues to respond to specific ITER concerns, now increasingly focused on development of the research plan. We report on two such areas of focused DIII-D research here.

5.1 Characterization of the L-H Threshold

A set of experiments was performed to determine H-mode access requirements for ITER's first (non-nuclear H and He) and second (activated D) operational phases. These experiments [42] build on previous work [43] demonstrating that threshold power P_{TH} increases with positive (parallel to I_p) rotation in both H and D plasmas. Similar behavior was confirmed in He plasmas. P_{TH} for the three species occurs approximately at the following ratios: P_{TH}(D:He:H) ≈ (1 : 1.4±0.1 : 2.1±0.1), with H-NBI → He lying between the two pure cases.

The density dependence of the H-mode power threshold is a key component of the ITPA2008 scaling [44]. Many devices, including DIII-D, observe a minimum in density that contrasts with this scaling. This minimum is seen in the new results (Fig. 15), in both D and He plasmas, albeit at different densities. Also, as previously observed, P_{TH} in He is higher than in D at low densities, with the difference decreasing with increasing density. H data is not included here since it was obtained at different current and field, but the above ratios are recovered when scaled according to the ITPA2008 toroidal field dependence.

Another finding of this study is the steady decrease in P_{TH} as the x-point moves closer to the divertor. This, combined with choosing the "right" density, may provide a
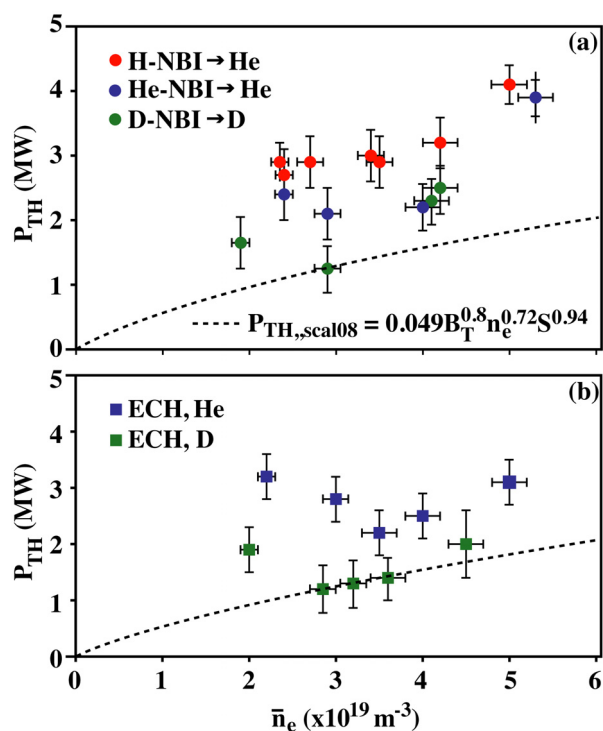

FIG. 15. The H-mode power threshold as a function of the line-integrated L-mode density for D and He plasmas (1.0 MA, 1.65 T) discharges with auxiliary heating by (a) NBI and (b) ECH. The dashed line corresponds to the ITPA2008 power threshold scaling relation for D plasmas.

path to obtain H-mode during the non-nuclear phase of ITER. These experiments also showed that activating the RMP ELM control coils increases the power threshold.

5.2 Predict the Impact of Test Blanket Modules (TBM) on ITER's Performance

ITER will include three pairs of toroidally-localized TBMs whose ferromagnetic structural materials will perturb the magnetic field. Theory to predict the impact of these field perturbations on performance is lacking, so DIII-D simulated the effect with a mockup (Fig. 16 inset) of a single TBM set with coils driving fields up to ~3× the relative amplitude of those in ITER. The TBM mock-up assembly was inserted in a midplane port on DIII-D for these experiments. It was subsequently removed, but can be reinserted for future experiments.

Measurements were made of the TBM's impact on parameters including L-H threshold, confinement, rotation, and energetic particles [45].

FIG. 16. Relative reductions of confinement factor H_{98} and toroidal velocity as a function of the local ripple δ. Below the ITER level, the mock-up's (see inset) effect on confinement was too small to measure.

The effect on rotation and confinement quality is shown in Fig. 16. Here, the local ripple $\delta \equiv (B_{max} - B_{min})/(B_{max} + B_{min})$ is the combined ripple arising from both the TBM and toroidal field coil non-axisymmetries. The equivalent value for ITER, in front of a TBM, is $\delta \approx 1.2\%$, and the DIII-D coil at full current (1.2 kA) is capable of reaching approximately 3.6%. In these experiments, we found only small effects on performance with the TBM mockup current set to match the ITER value. Decreased confinement and toroidal rotation were observed, but only when the coil current was increased to produce 2–3 times the ripple anticipated in ITER. Global losses of fast ions were small [46].

6. Summary and Future Research Directions.

We have described recent DIII-D research highlights in several areas; the references herein provide the reader a more complete discussion of these results.

Recent efforts to optimize steady-state scenarios extend the duration of fully noninductive high performance through tailoring of target conditions and "smart" application of external current drive. Aspects of other scenarios have been studied, including $\rho*$ scaling of Hybrid scenarios and generation of QH-mode without external torque. Safe access to and exit from ITER operating scenarios has been studied, with full discharge scenarios demonstrated in several different regimes. Future work will benefit from fast wave heating and additional ECH/CD both for tailoring profiles and establishing more reactor relevant conditions by primarily heating electrons. Off-axis NBI will provide additional control of the current profile.

Validation of physics-based models is a major emphasis across the DIII-D program. Here we described such efforts in transport, rotation, energetic particles, and the H-mode pedestal. These are given as examples; the approach of using modeling to design and interpret experiments permeates the DIII-D program. Future opportunities will take advantage of additional diagnostics, already commissioned and currently undergoing construction or upgrade.

Methods to control steady and transient particle and energy fluxes are extremely important to ensure the reliable operation and survivability of future devices. DIII-D is making important contributions in ELM control, disruption mitigation and avoidance, and controlling the particle inventory in the first wall.

The DIII-D research program has demonstrated strong interest and ability to respond to ITER's short and long term needs. Experiments with D, H, and He plasmas are contributing to plans for the initial operation of ITER, while at the same time producing a large dataset useful for confinement and transport research. Finally, DIII-D responded to an ITER-
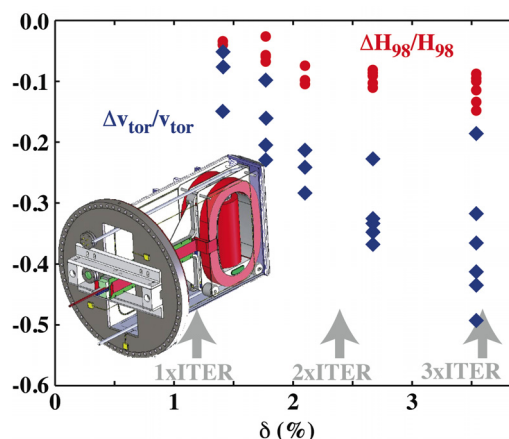
identified need for tests of the effects of the TBM on plasma performance, with the favorable result that at ITER equivalent perturbation strength, little or no degradation is seen in performance.

References

[1] FERRON, J.R., et al., this conference, EXS/P2-06
[2] HOLCOMB, C.T., et al., "Dependence of Transport on the Safety Factor Profile in DIII-D Steady-state Scenarios," Proc. of 37th EPS Conf. on Plasma Physics, Dublin, Ireland (2010) Paper P1.1108
[3] GREENFIELD, C.M., et al., Phys. Plasmas **11** (2004) 2616
[4] REIMERDES, H., et al., this conference, EXS/5-4
[5] IN, Y., et al., this conference, EXS/P5-07
[6] ROMANELLI, F., this conference, OV/1-3
[7] POLITZER, P.A., et al., this conference, EXC/P2-06
[8] JACKSON, G.L., et al., this conference, EXS/P2-11
[9] PARK, J.M., et al., this conference, EXC/P2-05
[10] RHODES, T.L., et al., this conference, EXC/7-2
[11] HOLLAND, C., et al., "Advances in Validating Gyrokinetic Turbulence Models in L and H mode Plasmas," to be presented at 52nd Am. Phys. Soc. Meeting of Division of Plasma Physics, Chicago, Illinois (2010)
[12] DeBOO, J.C., et al., Phys. Plasmas, accepted for publication (2010)
[13] SCHMITZ, L., et al., this conference, EXC/P7-01
[14] CANDY, J. and WALTZ, R.E., Phys. Rev. Lett. **91** (2003) 045001
[15] SOLOMON, W.M., et al., Nucl. Fusion **49** (2009) 085005
[16] SOLOMON, W.M., et al., this conference, EXC/3-5
[17] deGRASSIE, J.S., et al., Nucl. Fusion **49** (2009) 085020
[18] GURCAN, O.D., et al., Phys. Plasmas **14** (2007) 042306
[19] COLE, A.J., et al., "Observation of Peak Neoclassical Toroidal Viscous Force in the DIII-D Tokamak," submitted to Phys. Rev. Lett. (2010)
[20] GAROFALO, A.M., et al., Phys. Plasmas **16** (2009) 056119
[21] CALLEN, J.D., et al., Nucl. Fusion **49** (2009) 085021
[22] GREENFIELD, C.M., et al., Phys. Rev. Lett. PRL 2001
[23] BURRELL, K.H., Phys. Plasmas **8** (2001) 2153
[24] GAROFALO, A.M., et al., "Improving Stability and Confinement of Slowly Rotating Tokamak Plasmas Using Static Nonaxisymmetric Magnetic Fields," submitted to Phys. Rev. Lett. (2010)
[25] PACE, D.C., et al., this conference, EXW/4-2
[26] TOBIAS, B., et al., "Fast Ion Induced Shearing of Alfvén Eigenmodes Measured by 2D Electron Cyclotron Emission Imaging," submitted to Phys. Rev. Lett. (2010)
[27] SPONG, D.A., et al., Phys. Fluids B**4** (1992) 3316
[28] WHITE, R.B. and CHANCE, M.S., Phys. Fluids **27** (1987) 2455
[29] SNYDER, P.B., et al., this conference, THS/1-1
[30] OSBORNE, T.H., et al., this conference, EXC/2-1
[31] SNYDER, P.B., WILSON, H.R., and XU, X.Q., Phys. Plasmas **12** (2005) 056115
[32] SCHMITZ, O., et al., this conference, EXP/P3-30
[33] HUDSON, B., et al., this conference, EXC/P5-02
[34] YAN, Z., et al., this conference, EXC/P3-05
[35] PETRIE, T.W., et al., this conference, EXD/P3-27
[36] BAYLOR, L.R., et al., "ELM Pacing by Pellet Injection on DIII-D and Extrapolation to ITER," Proc. of 37th EPS Conf. on Plasma Physics, Dublin, Ireland, 2010, P2.117
[37] IZZO, V.A., et al., this conference, THS/9-2
[38] COMMAUX, N., et al., this conference, EXS/P2-02
[39] WESLEY, J.C., et al., Proc. 22nd IAEA Fusion Energy Conf., Geneva (2008) Paper EX/7-3Rb
[40] JAMES, A.N., et al., "Pellet Interaction with Runaway Electrons," accepted for publication in J. Nucl. Mater. (2010).
[41] ALLEN, S.L., et al., this conference, EXD/6-4
[42] GOHIL, P., et al., this conference, EXC/2-4Ra
[43] GOHIL, P., et al., Nucl. Fusion **49** (2009) 115004
[44] MARTIN, Y.R., et al., J. of Physics: Conf. Series **123** (2008) 012033
[45] SCHAFFER, M.J., et al., this conference, ITR/1-3
[46] KRAMER, G.J., et al., this conference, EXW/P7-10

APPENDIX: THE DIII-D TEAM

G. Abla,[1] M.M. Abrahim,[1] E.O. Allen,[1] S.L. Allen,[2] D.D. Anastasi,[1] P.M. Anderson,[1] M.E. Austin,[6] F.W. Baity,[4] J.P. Bakalarski,[1] C.P. Balance,[5] I. Balboa,[6] E.M. Bass,[7] D.J. Battaglia,[4] C.B. Baxi,[1] L.R. Baylor,[4] M. Becoulet,[8] E.A. Belli,[7] J.W. Berkery,[9] L.A. Berry,[4] M.N.A. Beurskens,[6] J.M. Bialek,[9] J.A. Boedo,[10] I.N. Bogatu,[11] R.L. Boivin,[1] P. Bonoli,[12] A.H. Boozer,[9] B.D. Bray,[1] D.P. Brennan,[5] S. Brezinsek,[14] N.H. Brooks,[1] D. Buchenauer,[15] R.V. Budny,[16] R. Bulmer,[2] P. Burratti,[11] K.H. Burrell,[1] R.J. Buttery,[1] J.D. Callen,[18] R.W. Callis,[1] G.L. Campbell,[1] J.M. Candy,[1] J.M. Canik,[4] T.N. Carlstrom,[1] T.A. Carter,[19] W.P. Cary,[1] T.A. Casper,[2] M. Cengher,[1] C.D. Challis,[6] F.R. Chamberlain,[1] V.S. Chan,[1] M.S. Chance,[16] C.S. Chang,[20] J.A. Chavez,[1] B. Chen,[1] R. Chipman,[21] H.K. Chiu,[1] M. Choi,[1] C. Chrobak,[1] C. Chrystal,[10] M.S. Chu,[1] V. Chuyanov,[22] I.G.J. Classen,[23] A.J. Cole,[18] N. Commaux,[4] F. Crisanti,[17] N.A. Crocker,[19] G. Cunningham,[6] D.S. Darrow,[16] J.W. Davis,[24] E. de la Luna,[25] P. de Vries,[23] J.C. DeBoo,[1] J.S. deGrassie,[1] S.J. DePasquale,[16] T.M. Deterly,[1] P.H. Diamond,[10] J.L. Doane,[1] C.W. Domier,[26] J. Dorris,[12] E.J. Doyle,[19] K. Dubovenko,[1] J. Edwards,[16] T. Eich,[27] N.W. Eidietis,[1] J.D. Elder,[24] R. Ellis,[2] R.A. Ellis,[16] R.F. Ellis,[28] A.L. Equizabal,[16] T.E. Evans,[1] M.E. Fenstermacher,[2] J.R. Ferron,[1] D.K. Finkenthal,[29] R.K. Fisher,[1] B.W.N. Fitzpatrick,[24] S.M. Flanagan,[1] J. Flanagan,[6] R.J. Fonck,[18] L. Frassinetti,[30] E. Fredd,[16] E.D. Fredrickson,[16] H.G. Frerichs,[14] C. Fuchs,[27] S. Gao,[31] X. Gao,[31] M. García-Muñoz,[27] A.M. Garofalo,[1] D.A. Gates,[16] R. Geer,[2] K.W. Gentle,[3] A. Geraud,[8] S. Gerhardt,[16] E. Giovannozzi,[32] C. Giroud,[6] P. Gohil,[1] N.N. Gorelenkov,[16] Y.A. Gorelov,[1] R.H. Goulding,[4] R.S. Granetz,[12] D.L. Green,[4] K.L. Greene,[1] C.M. Greenfield,[1] N.L. Greenough,[16] Y. Gribov,[22] B.A. Grierson,[16] R.J. Groebner,[1] W.H. Grosnickle,[1] M. Groth,[2, 47] H.J. Grunloh,[1] W. Guo,[31] T.J. Guzman,[1] A.A. Haasz,[24] T.S. Hahm,[16] S.H. Hahn,[33] J. Hansink,[1] G.R. Hanson,[4] J.M. Hanson,[9] R.W. Harvey,[34] A. Hassanein,[35] C.C. Hegna,[18] W.W. Heidbrink,[36] A. Herrmann,[27] D.N. Hill,[2] J.C. Hillescheim,[19] D.L. Hillis,[4] J.K. Hobirk,[27] C.T. Holcomb,[2] C. Holland,[10] E.M. Hollmann,[10] K.L. Holtrop,[1] R.M. Hong,[1] A.R. Horton,[4] L.D. Horton,[27] J.C. Hosea,[16] J. Howard,[37] D.M. Hoyt,[1] C.L. Hsieh,[1] A. Huber,[14] B. Hudson,[7] J.W. Hughes,[12] D.A. Humphreys,[1] P. Huynh,[1] G.T.A. Huysmans,[8] A.W. Hyatt,[1] S. Ide,[38] F. Imbeaux,[8] Y. In,[11] R.C. Isler,[4] V.A. Izzo,[10] S. Jachmich,[39] G.L. Jackson,[1] W. Jacob,[27] E.F. Jaeger,[4] M.W. Jakubowski,[40] A.N. James,[10] R.J. Jayakumar,[1] I. Jenkins,[6] Y.M. Jeon,[41] T.C. Jernigan,[4] H. Jhang,[33] E.H. Joffrin,[8] R.D. Johnson,[1] P. Johnson,[42] I. Joseph,[2] A. Kallenbach,[27] R.C. Kalling,[1] D.H. Kaplan,[1] O. Katsuro-Hopkins,[9] S.M. Kaye,[16] K.M. Keith,[1] A.G. Kellman,[1] D.H. Kellman,[1] M. Kempenaars,[6] C.E. Kessel,[16] E.N. Kim,[1] L. Kim,[1] J.S. Kim,[11] S.H. Kim,[43] J.D. King,[44] J.E. Kinsey,[1] A. Kirk,[6] A. Kirschner,[14] F. Kochl,[45] N. Kohen,[46] C. Konz,[40] T. Koskela,[47] G.J. Kramer,[16] S.I. Krasheninnikov,[10] K. Krieger,[27] J.A. Kulchar,[1] T. Kurki-Suonio,[47] R.J. La Haye,[1] B. LaBombard,[12] R. Laengner,[14] M.J. Lanctot,[2] L.L. Lao,[1] C.J. Lasnier,[2] E.A. Lazarus,[4] R.L. Lee,[1] X. Lee,[1] A.W. Leonard,[1] J.A. Leuer,[1] G.Q. Li,[31] Z. Lin,[36] A. Litnovsky,[14] C. Liu,[1] Y.Q. Liu,[6] D. Liu,[18] S. Liu,[31] A. Loarte,[22] S.D. Loch,[5] L.L. Lodestro,[2] N. Logan,[48] J. Lohr,[1] P. Lomas,[6] J. Lonnroth,[47] T.C. Luce,[1] N.C. Luhmann Jr.,[26] G. Maddison,[6] C.F. Maggi,[27] M.A. Mahdavi,[49] R. Maingi,[4] M.A. Makowski,[2] M. Marot,[50] L. Marrelli,[32] P. Martin,[32] D. Mastrovito,[16] G. Matsunaga,[38] P.S. Mauzey,[1] D.C. McCune,[16] W.L. McDaniel,[1] D.C. McDonald,[6] B.B. McHarg,[1] G.R. McKee,[18] A.G. McLean,[4] J.E. Menard,[16] W.H. Meyer,[2] O. Meyer,[51] D. Mikkelsen,[16] D.C. Miller,[1] C.P. Moeller,[1] S. Mordijck,[10] K. Morris,[2] E.C. Morse,[44] R.A. Moyer,[10] Y.R. Mu,[24] D. Mueller,[16] S.H. Müller,[10] H.W. Müller,[27] J.M Muñoz Burgos,[7] M. Murakami,[4] C.J. Murphy,[1] C.M. Muscatello,[36] A. Nagy,[16] E. Nardon,[8] M.F.F. Nave,[52] G.A. Navratil,[9] R. Nazikian,[16] H. Nehme,[8] J. Neilson,[53] S. Noraky,[1] I. Nunes,[54] R.E. Nygren,[15] R.C. O'Neill,[1] Y.K. Oh,[33] M. Okabayashi,[16] R.A. Olstad,[1] G.M. Olynyk,[12] D.M. Orlov,[10] T.H. Osborne,[1] Y. Ou,[41] L.W. Owen,[4] N. Oyama,[38] N.A. Pablant,[10] D.C. Pace,[36] C. Pan,[31] A.Y. Pankin,[41] J.M. Park,[4] J.K. Park,[16] G. Park,[20] H.K. Park,[55] C.T. Parker,[1] P.B. Parks,[1] R. Pasqualotto,[17] C.J. Pawley,[1] L.D. Pearlstein,[2] W.A. Peebles,[19] B. Pegourie,[8] B.G. Penaflor,[1] P.I. Petersen,[1] T.W. Petrie,[1] C.C. Petty,[1] N.Q. Pham,[1] V. Philipps,[14] D.A. Piglowski,[1] R.I. Pinsker,[1] P. Piovesan,[32] L. Piron,[32] R.A. Pitts,[22] P.A. Politzer,[1] D.M. Ponce,[1] M. Porkolab,[12] G.D. Porter,[2] A. Pospieszczyk,[14] R. Prater,[1] V.D. Pustovitov,[56] J.P. Qian,[31] N. Ramasubramanian,[57] D.A. Rasmussen,[4] H. Reimerdes,[9, 58] D. Reiter,[14] Q.L. Ren,[31] M.E. Rensink,[2] T.L. Rhodes,[19] H. Rinderkhecht,[16] T.D. Rognlien,[2] G. Rossi,[16] J.C. Rost,[12] D.L. Rudakov,[10] P.M. Ryan,[4] D. Ryutov,[2] S. Saarelma,[6] S.A. Sabbagh,[9] G. Saibene,[59] A. Salmi,[47] U. Samm,[14] B.S. Sammuli,[1] R. Sartori,[59] O. Sauter,[58] R.I. Savercool,[1] M.J. Schaffer,[1] D.P. Schissel,[1] D.J. Schlossberg,[18] O. Schmitz,[14] L. Schmitz,[19] E. Schuster,[41] E. Scime,[60] J.T. Scoville,[1] M.W. Shafer,[18] M. Shapiro,[12] J.P. Sharpe,[61] K. Shinohara,[38] K.C. Shoolbred,[1] P.E. Sieck,[1] A.C.C. Sips,[27] R.D. Smirnov,[10] J.P. Smith,[1] S. Smith,[1] J.A. Snipes,[22] P.B. Snyder,[1] E.R. Solano,[25] W.M. Solomon,[16] A.C. Sontag,[4] A. Soppelsa,[32] K.H. Spatschek,[62] D.A. Spong,[4] R. Srinivasan,[57] H.E. St. John,[1] W.M. Stacey,[63] G.M. Staebler,[1] R.D. Stambaugh,[1] P.C. Stangeby,[24] R. Stemprok,[1] T. Stevenson,[16] H. Stoschus,[14] E.J. Strait,[1] R.W. Street,[1] W. Suttrop,[27] T. Suzuki,[27] V. Svidzinski,[11] T. Tala,[64] D.A. Taussig,[1] P.L. Taylor,[1] T.S. Taylor,[1] D.M. Thomas,[1] B.J. Tobias,[26] J.F. Tooker,[1] C.K. Tsui,[24] F. Turco,[7] A.D. Turnbull,[1] G.R. Tynan,[10] M. Umansky,[2] K.R. Umstadter,[10] E.A. Unterberg,[4] I.U. Uzun-Kaymak,[18] M.A. Van Zeeland,[1] S. Visser,[1] F. Volpe,[18] A. von Halle,[16] M.R. Wade,[1] M.L. Walker,[1] M. Walsh,[6] R.E. Waltz,[1] W.R. Wampler,[15] B.N. Wan,[31] G. Wang,[19] H.Z. Wang,[31] J.G. Watkins,[15] A.S. Welander,[1] J.C. Wesley,[1] W.P. West,[1] A.E. White,[12] R.B. White,[16] D.G. Whyte,[12] S. Wiesen,[14] J.R. Wilson,[16] H.R. Wilson,[65] A. Wingen,[62] M. Wischmeier,[27] R.C. Wolf,[40] E. Wolfrum,[27] C.P.C. Wong,[1] S.K. Wong,[66] W. Wu,[1] S.J. Wukitch,[12] B.J. Xiao,[31]

X. Xu,[2] Z. Yan,[18] H.H. Yip,[1] S-W. Yoon,[33] K-I. You,[33] D. Young,[67] J.H. Yu,[10] Q.P. Yuan,[31] L. Zabeo,[6] D. Zarzoso,[68] L. Zeng,[19] W. Zhang,[19] Y.B. Zhu[36]

AFFILIATIONS

[1] General Atomics
[2] Lawrence Livermore National Laboratory
[3] University of Texas
[4] Oak Ridge National Laboratory
[5] Auburn University
[6] EURATOM/CCFE Fusion Association, Culham Science Centre
[7] Oak Ridge Institute of Science Education
[8] Association Euratom CEA, DSM/IRFM, Cadarache
[10] University of California, San Diego
[11] Columbia University
[11] FAR-TECH, Inc.
[12] Massachusetts Institute of Technology
[13] University of Tulsa
[14] EURATOM-FZ Jülich
[15] Sandia National Laboratories
[16] Princeton Plasma Physics Laboratory
[17] ENEA-Frascati
[18] University of Wisconsin
[19] University of California, Los Angeles
[20] Courant Institute, New York University
[21] University of Arizona
[22] ITER Organization, Cadarache
[23] Association EURATOM-FOM Rijnhuizen, The Netherlands
[24] University of Toronto
[25] Association EURATOM-CIEMAT, Madrid
[26] University of California, Davis
[27] Max Plank Institut für Plasmaphysik, Garching
[28] University of Maryland
[29] Palomar College
[30] Association EURATOM-VR, Alfven Laboratory, Stockholm
[31] ASIPP-Hefei
[32] Consorzio RFX
[33] National Fusion Research Institute, Korea

[34] CompX
[35] Purdue University
[36] University of California, Irvine
[37] Australian National University
[38] Japan Atomic Energy Agency (JAEA)
[39] Association EURATOM, Belgium
[40] Max Plank Institut für Plasmaphysik, Greifswald
[41] LeHigh University
[42] Butler University
[43] Korea Atomic Energy Research Institute
[44] University of California, Berkeley
[45] Association EURATOM-OAW/ATI, Vienna
[46] University of Marseille, France
[47] Helsinki University of Technology
[48] Brown University
[49] ALITRON
[50] University of Basel, Switzerland
[51] Association Euratom CEA, DSM/IRFM, Cadarache
[52] EURATOM Lisbon
[53] Lexam Research, Redwood City
[54] Association EURATOM-IST, Lisbon
[55] Pohang University of Science & Technology, Korea
[56] Institute for Tokamak Physics, Moscow
[57] Institute for Plasma Research, India
[58] CRPP-EPFL-Lausanne
[59] Fusion for Energy Joint Undertaking, Barcelona
[60] West Virginia University
[61] Idaho National Laboratory
[62] Heinrich-Heine University, Düsseldorf
[63] Georgia Institute of Technology
[64] Association EURATOM-Tekes, Finland
[65] University of York
[66] Mesa College
[67] National Renewable Energy Laboratory, USA
[68] Ecole Polytechnique, France